3D-Printing of Highly Piezoelectric Barium Titanate Polymer Nanocomposites with Surface-Modified Nanoparticles at Low Loadings

Mirko Maturi, Lorenzo Migliorini, Sara Moon Villa, Tommaso Santaniello, Natalia Fernandez-Delgado, Sergio Ignacio Molina, Paolo Milani,* Alberto Sanz de León,* and Mauro Comes Franchini*

This work describes the development and characterization of tetragonal barium titanate nanoparticles (BTO NPs) and their surface functionalization with dopamine dodecylamine (DDA), a lipophilic organic ligand. The so-obtained lipophilic NPs (BTO-DDA) are then formulated at low loadings (< 5 wt.%) into liquid photocurable resins for vat photopolymerization (VP) and 3D printed into solid objects. The printed composites are mechanically characterized in order to assess the effect of the nanomaterial on the mechanical properties of the 3D printed polymer, revealing no significant variations in the mechanical properties (tensile or flexural) of the nanocomposites compared to the original polymer matrix. In light of these results, the printed nanocomposites are studied in terms of their capacity to generate a separation of charge by the piezoelectric effect, typical of the BTO crystal structure. This study reveals that BTO-loaded nanocomposites display outstanding piezoelectric coefficients as high as 50 pC/N when BTO-DDA is formulated at 3.0 wt.%, only slightly less than one-third of the piezoelectric coefficient previously reported for bulk BTO, while preserving the mechanical properties of the polymer matrix.

M. Maturi, N. Fernandez-Delgado, S. I. Molina, A. Sanz de León
Dpto. Ciencia de los Materiales
I. M. y Q. I.
IMEYMAT
Facultad de Ciencias
Universidad de Cádiz
Campus Río San Pedro, s/n, Puerto Real, Cadiz 11510, Spain
E-mail: alberto.sanzdeleon@uca.es
M. Maturi, M. C. Franchini
Department of Industrial Chemistry "Toso Montanari"
V. Piero Gobetti 85, Bologna 40129, Italy
E-mail: mauro.comesfranchini@unibo.it
L. Migliorini, S. M. Villa, T. Santaniello, P. Milani
CIMAINA and Dipartimento di Fisica
Università degli Studi di Milano
via Celoria 16, Milano 20133, Italy
E-mail: paolo.milani@mi.infn.it

1. Introduction

In the latest years, additive manufacturing (AM, also known as 3D-printing), has become the most versatile and customizable object manufacturing technique in various fields, including medical devices, automotive, aerospace, and jewelry, thanks to its many advantages compared to traditional subtractive manufacturing techniques.[1–3] In particular, AM allows for improved and faster production customizability and reduced material waste, features that are continuously increasing the possibilities of AM for applications at the industrial scale.[4,5] Over the years, different types of 3D printing technologies have been developed, such as vat photopolymerization (VP), selective laser sintering (SLS), and fused deposition modeling (FDM), which differ by the technique employed for the deposition of material layers and from the type of materials used, including polymers, ceramics, glasses, and metals.[6] Amongst the different 3D printing techniques available, VP is attracting the interest of the scientific community thanks to its ability to deal with liquid photopolymer resins which are selectively hardened by means of UV–vis light to afford solid objects with high resolution and precision of details, and materials with a wide range of mechanical properties.[7,8] Nonetheless, the liquid nature of resins for VP applications has allowed for the incorporation of functional nanomaterials, which lead to 3D printed solid nanocomposite materials possessing functional properties such as optical absorption, mechanical strengthening, magneticity, electrical conductivity, and piezoelectricity, amongst others.[9,10] Due to the lipophilic organic environment typical of acrylate and methacrylate resins, surface modification of nanomaterials is needed to improve the compatibility of the nanofiller with the liquid photopolymer matrix.[11] The type of surface modification is strongly related to the surface chemistry of the nanomaterial and to the nature of the matrix, as well as the type of interaction required to maximize the transfer of the functional properties from the nanomaterial to the nanocomposite.[12] As an example, when the incorporation of nanofillers is performed to improve the mechanical properties of materials, a covalent

bond between the nanomaterial and the polymer matrix is often preferred, as it allows for seamless transmission of mechanical stress from the matrix to the filler.[13–15] In contrast, when utilizing fillers with different functionalities, it is recommended to employ a non-reactive and lipophilic coating to enhance the dispersibility of the nanomaterial and prevent aggregation.[16–18] Amongst the different functionalities that nanofillers dispersed in polymer matrices can confer to the composite materials, piezoelectricity is one of great interest, as it allows for the manufacturing of pressure sensors and energy harvesting devices with applications spanning from organic electronics to smart biomedical devices.[19,20] Piezoelectric materials are, in fact, able to convert mechanical stress into a separation of electric charge, which can be either measured (for sensing applications) or collected and stored (for energy harvesting applications).[21] For this reason, the research community is focusing great attention onto the inclusion of piezoelectric materials into photocurable resins for vat photopolymerization, in order to combine the advantages of photopolymerization-based AM (such as high resolution and versatility) with the piezoelectric properties of nanomaterials, with the aim of building customizable piezoelectric nanocomposites for a wide range of applications.[22,23] The main piezoelectric nanocomposites reported so far for VP contain ceramic (nano)perovskites that display piezoelectricity at room temperature, such as barium titanate ($BaTiO_3$, BTO) and lead zirconium titanate ($Pb[Zr_xTi_{1-x}]O_3$, PZT).[24,25] PZT has higher piezoelectric coefficients and wider range of compatible temperatures than BTO. Specifically, PZT maintains its piezoelectricity up to 300–350 °C, while BTO loses its piezoelectric properties at ≈120–130 °C. However, polymer nanocomposites for energy harvesting and mechanical sensing are typically utilized below 100 °C, a temperature at which BTO still maintains its piezoelectric potential.[26,27] Moreover, PZT contains toxic heavy metals such as lead (Pb) in amounts above 60 wt.%, leading to environmental pollution during production and posing harmful effects to the human body. This fact impedes the potential application of PZT nanocomposites in the fields of biomedicine and wearable electronics, where BTO has demonstrated significant potential in recent literature due to its biocompatibility, safety and cheap manufacturing.[28–30] In most cases, when formulated with photocurable resins for the production of piezoelectric 3D structures, BTO is added at high concentration (> 40 wt.%) in order to lead to 3D printed composites that are successively sintered at high temperature to burn the organic polymer matrix therefore achieving bulk ceramic materials that possess high temperature stability and good piezoelectricity (reaching d_{33} values as high as 160 pC/N) but mechanical properties typical of ceramic materials such as high fragility and low deformability.[31–33] To overcome these limitations, researchers are exploring the possibility of producing piezoelectric nanocomposite materials with low BTO contents (< 5 wt.%) with the aim of obtaining composite materials with the highest possible piezoelectricity while preserving the mechanical behavior of polymeric materials. To the best of our knowledge, polymer nanocomposites displaying good piezoelectric coefficients (> 20 pC/N) with low BTO contents in non-piezoelectric polymer matrices have never been reported yet, neither produced by traditional manufacturing techniques, nor by additive manufacturing approaches.

In this work, we report the formulation and AM fabrication of piezoelectric nanocomposites using dopamine dodecylamide (DDA)-modified BTO nanoparticles embedded at low loadings (0.1–5 wt.%) in photocurable resins for vat photopolymerization. The liquid photoresins were 3D printed by means of VP into nanocomposite materials covering a wide range of mechanical properties, then poled to induce the dipole alignment in the embedded nanoparticles. This process generated the piezoelectric properties that were further quantified by evaluating the corresponding d_{33} coefficients at different stimulation frequencies, revealing outstanding piezoelectricity with d_{33} values reaching one third of the ones of bulk BTO with loading as low as 3.0 wt.%.

2. Results and Discussion

2.1. Synthesis and Characterization of BTO and BTO-DDA NPs

Thanks to the good piezoelectric performances that DDA-coated BTO NPs have demonstrated in a previously published work when formulated in PDMS matrix,[34] BTO and BTO-DDA have been prepared with an analogous approach, and independently characterized to assess the reproducibility of the previously reported methods (**Figure 1a**). First, XRD analysis was employed to assess the crystallinity of the nanomaterials, confirming the expected crystal structure for both BTO and BTO-DDA, suggesting that surface functionalization with DDA did not affect the BTO internal crystal structure (Figure 1b). BTO display a non-piezoelectric cubic crystal structure stable above its Curie temperature (133 °C), but at room temperature the crystal lattice distorts leading to the less symmetric piezoelectric tetragonal phase, causing a splitting in the XRD reflection peaks.

However, the XRD peak broadening related to the small particle size does not allow for the unambiguous identification of the XRD reflections of the piezoelectric tetragonal phase of BTO crystals. Nonetheless, this phase is to be expected due to its higher thermodynamic stability at room temperature and it will be confirmed by the piezoelectric properties measured in the following paragraphs. TEM confirmed the expected size and morphology previously reported for NPs prepared with this method, showing small crystallites (20–50 nm) aggregated into larger particles. (Figure 1c). Finally, TGA was performed to assess the amount of DDA efficiently bound to BTO NPs (Figure S1, Supporting Information), which revealed that the nanosystem is composed of 87 wt.% BTO and 13 wt.% of organic matter.

2.2. Formulation and 3D Printing of BTO-Loaded Resins

The prepared nanoparticles were dispersed in the photocurable resin R1 to produce liquid composite resins able to be photocured into 3D shapes by means of vat photopolymerization. The list of prepared samples and their composition is reported in **Table 1**, together with the acronyms used to identify each formulation. When the nanofiller concentration was increased above 3.5 wt.% for BTO and 5 wt.% for BTO-DDA, the NPs remained larger aggregates, visible by the naked eye. Part of these aggregates adhered to the walls and the bottom of the container of the resin precursor and most of it sedimented at the bottom of the resin after
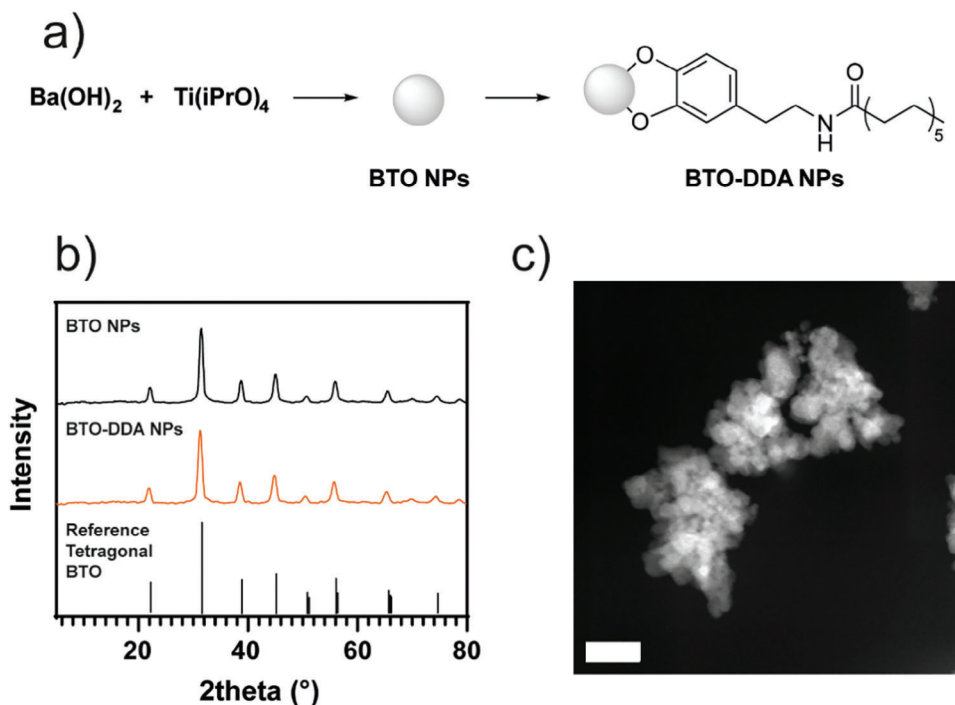
Figure 1. Synthesis and characterization of BTO-DDA NPs. a) Reaction scheme for the synthesis and functionalization of BTO NPs. b) XRD spectrum of BTO, BTO-DDA and reference reflection peaks for tetragonal BTO crystals.[35] c) STEM-HAADF image of BTO-DDA NPs (scale bar = 50 nm).

a few hours. Attempts to disperse these aggregates by increasing the stirring or sonication time did not lead to any enhancement. In fact, increasing the stirring speed was counterproductive since it only led to an increase in the formation of bubbles. Thus, these concentrations (3.5 wt.% for BTO and 5 wt.% for BTO-DDA) were set as the upper threshold to manufacture the materials with a homogeneous distribution of the nanofiller.
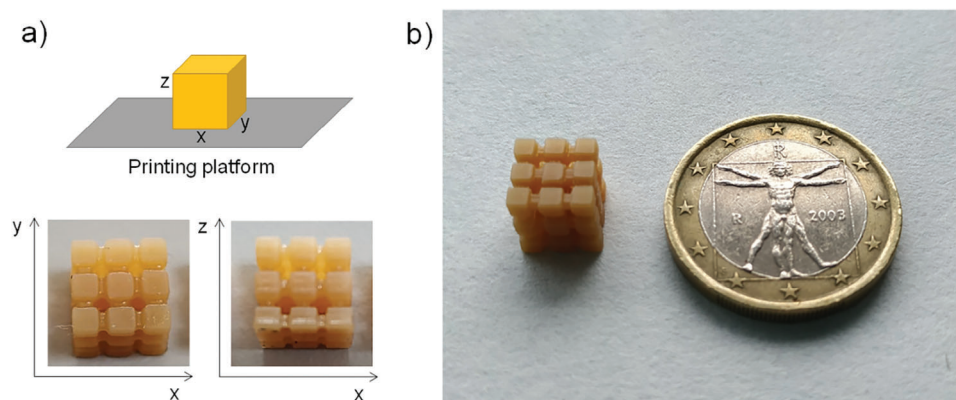
Furthermore, the formulated nanocomposite resins underwent rheological analysis to assess the effect of the presence of modified and unmodified BTO NPs on the resins' viscosity (Figure S2, Supporting Information). The analysis revealed that BTO-DDA did not affect significantly the viscosity of the photocurable resins, which remained constant at ≈1 Pa·s at all concentrations showing Newtonian behavior. On the other hand, the poor dispersibility of unmodified BTO and the related presence of larger aggregates had a dramatic effect on the viscosity at low shear rates. These findings suggest once again how the improved dispersibility of BTO-DDA thanks to its surface modification is beneficial for the formulation of photocurable nanocomposite resins and explains their greater printability. In fact, the nanofiller loadings reported in Table 1 allowed for successful 3D printing of the nanocomposites in all cases (see

Figures S3 and S4, Supporting Information), including complex structures with gap and other submillimetric details, as shown in **Figure 2**, where a concentration of 5.0 wt.% BTO-DDA was used.

All the discs printed with either BTO or BTO-DDA nanocomposites were translucent, increasing their opacity as the amount of BTO NPs increases (**Figure 3**). This indicates that the BTO NPs are homogeneously distributed within the resin, but likely in the form of aggregates able to scatter visible light. Furthermore, composites containing DDA-functionalized nanoparticles were characterized by an orange-brown color, generated by the surface-bound catechol functionality, as previously reported.[34,36] We further investigated this aspect by recording the UV–vis transparency of 3D printed discs (Figure S5, Supporting Information). Interestingly, the R1-D5 printed composites were more transparent than the corresponding R1-B5, thus confirming the higher dispersibility and lower aggregate size expected for lipophilic DDA-functionalized nanoparticles. In fact, according to Nussbaumer equation, optimized for nanocomposites from the Rayleigh scattering theory, increasing the dispersion of particles within the polymer matrix reduces the average size of nanoparticles without affecting their volume fraction in the composite. This ultimately leads to increased transmittance.[37] When 3.5 wt.% BTO was used (R1-B35), larger aggregates were visible by naked eye, as shown in Figure 3f. This did not interfere with the printing of this nanocomposite (see Figure S3, Supporting Information) but evidences the lower ability of the unmodified BTO NPs to be dispersed in the R1 matrix due to their polar hydroxylated surface, which poorly interacts with the acrylate monomers that compose the photocurable resin. In fact, the stabilizing effect of long aliphatic chains, promoting a better

Table 1. Composition and designation of the prepared liquid nanocomposites using R1 resin.

	R1	R1-B5	R1-B35	R1-D5	R1-D10	R1-D30	R1-D50
BTO	–	0.5 wt.%	3.5 wt.%	–	–	–	
BTO-DDA	–	–	–	0.5 wt.%	1.0 wt.%	3.0 wt.%	5.0 wt.%

Figure 2. a) Schematic representation and digital pictures of a hollow cubic lattice observed from different planes, illustrating the high resolution; b) comparison of the printed object with a coin to illustrate its size. The structure was printed using resin R1-D50.

dispersion of the additive in the resin matrix, was previously observed by some of us in cellulose nanocrystals nanocomposites for vat photopolymerization.[18] However, due to its orange color, we believed it was worth investigating whether the presence of DDA in the commercial photocurable formulation could affect the photopolymerization reaction during 3D printing, thus leading to structural differences in the BTO-DDA loaded composites. To do so, the formulated nanocomposite resins were subjected to UV–vis spectroscopy as 2 vol% solutions in DMF (0.1 mL of resin in 5 mL of DMF in a 10 mm cuvette) revealing no significant differences between the UV extinction properties of resins R1-B5 and R1-D5 at 405 nm, the wavelength of the light source of the employed 3D printing system (Figure S6, Supporting Information). The tested concentration was selected to mimic the optical behavior of a 0.2 mm-thick layer of photocurable resin, revealing that, for both R1-B5 and R1-D5, ≈15% of the incident light was transmitted at 405 nm when irradiating a layer of resin which is four times the thickness employed for the 3D printing process. Furthermore, ATR-FTIR revealed

that resin R1 was fully photocured right after printing (Figure S7a, Supporting Information) as well as all the nanocomposite formulations, which showed no appreciable differences in their FTIR spectra (Figure S7b, Supporting Information).

In particular, this is revealed by the stable reduction in the intensity of the photocurable C=C vibration absorption band (809 cm^{-1}) after printing, which is not affected by any further post-curing process or addition of nanoparticles. Usually, for photocurable compositions, additional bands related to the photocurable C=C vibration bands are monitored at ≈1636 and 1410 cm^{-1}. However, using commercial photocurable formulations with unknown composition made it impossible in this case, due to the overlap of such C=C signal with additional IR bands.[38]
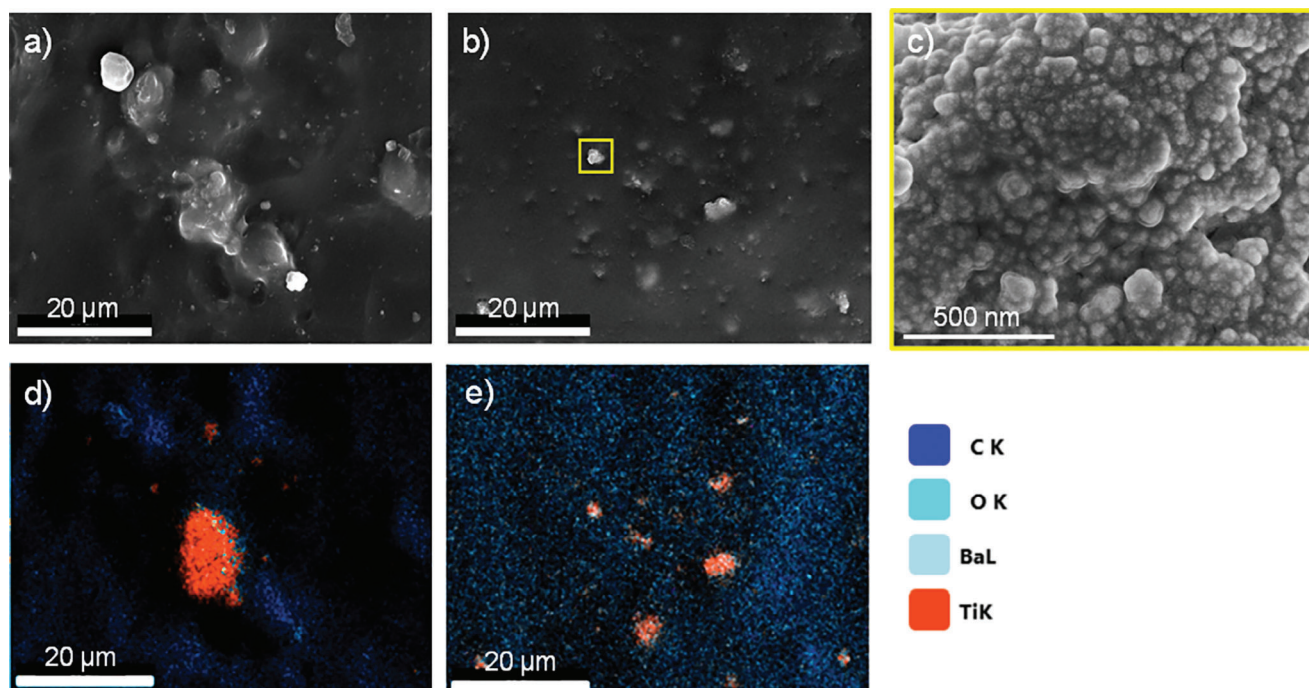
Therefore, it can be concluded that the presence of DDA does not interfere with the light absorption properties of the photocurable mixture, and thus with the extent of its polymerization.

To gain further insights of the distribution of the BTO NPs and the microstructure of these nanocomposites, SEM studies were carried out on the surface of some of the printed objects.
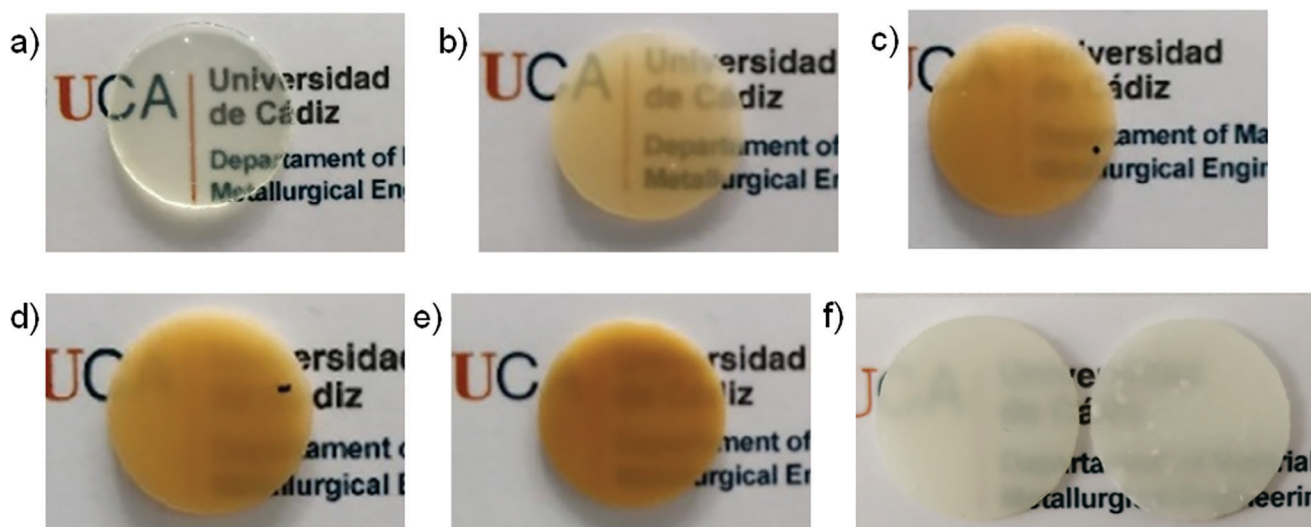
Figure 3. a) Digital photographs of 1-mm thick flat discs printed with a) R1; b) R1-D5; c) R1-D10; d) R1-D30, e) R1-D50 and f) R1-B5 (left) and R1-B35 (right).

**ADVANCED
SCIENCE NEWS**

www.advancedsciencenews.com

**ADVANCED
FUNCTIONAL
MATERIALS**

www.afm-journal.de

Figure 4. SEM micrographs of 3D printed a) R1-B5 and b-c) R1-D5 nanocomposites. EDX mappings of a) and b) are shown in d) and e) respectively.
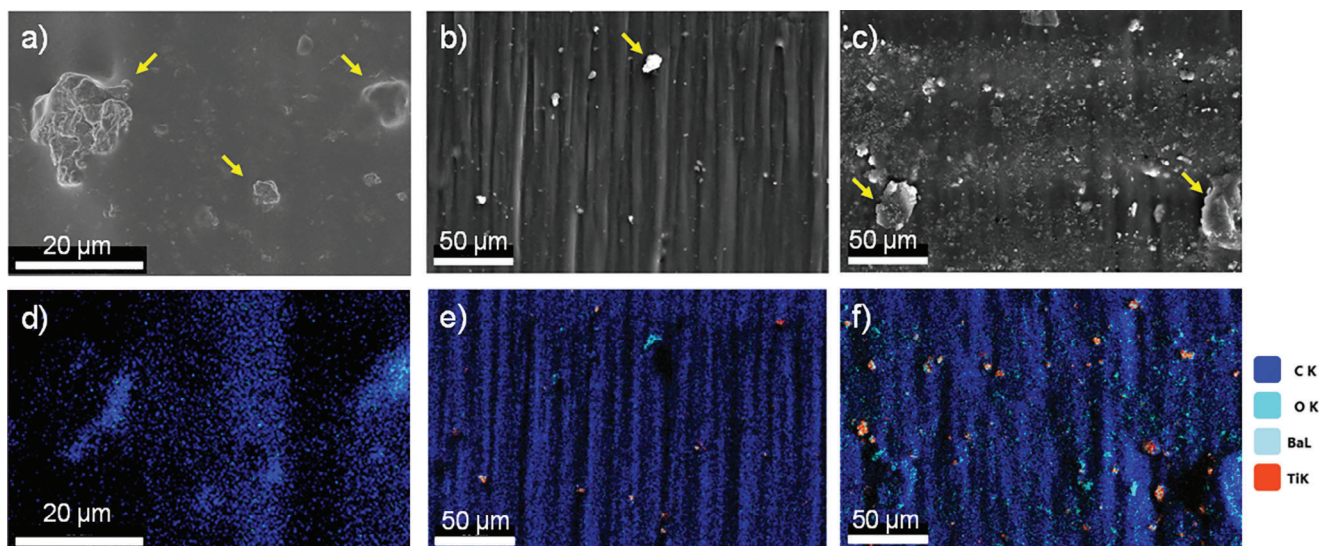
Figure 4 shows a comparison of the surface morphologies of R1-B5 and R1-D5 nanocomposites. Both SEM images show a rough surface, with what seem particle aggregates with sizes of several microns. In the case of the BTO-DDA nanocomposites, these aggregates look smaller and more homogeneously distributed within the resin, as Figure 3 suggested. A closer look at these aggregates reveals that they are composed of individual BTO-DDA NPs (Figure 4c), which have an average size of 48 ± 14 nm, in agreement with TEM images. However, the EDX mappings (Figure 4d,e; Figure S8, Supporting Information) show that not all the protrusions observed in the surface of the SEM images correspond to the presence of either BTO or BTO-DDA. The EDX signals from Ba and Ti clearly show that the aggregates in R1-B5 nanocomposites are larger than in R1-D5 nanocomposites, but they do not necessarily match the contrasts observed in the SEM images. Comparing the EDX mappings, it can be clearly observed that BTO-DDA are better dispersed, in the form of smaller structures than in the case of the BTO nanocomposite, where only one significantly bigger aggregate is only observed.

A more detailed analysis is presented in **Figures 5** and S9 (Supporting Information), where SEM images and EDX mappings are compared for 3D printed R1, R1-D5 and R1-D30 nanocomposites. Interestingly, the SEM image of R1 shows surface morphologies what could be ascribed to the presence of BTO NPs (or any kind of particles in general). However, the EDX mapping unequivocally show that this must be due to the surface roughness of the resin itself, since it only displays EDX signals corresponding to C and O (and Au due to the sputter coating, not included in the mapping). This also happens, to a lesser extent, in the case of the BTO-DDA nanocomposites, where a few of the particles observed do not show any Ti or Ba signal in the EDX mappings, as indicated in Figure 5a–c with yellow arrows. Hence, it is impor-

tant to notice that not all the aggregates observed in the SEM images may be correlated with the presence of BTO (or BTO-DDA) NPs. The EDX mappings of the BTO-DDA nanocomposites show that when the BTO-DDA content is increased, the number and size of micron-sized aggregates increases slightly. The average size was measured from the EDX images, and it was found that varies from 2.2 ± 1.2 µm for R1-D5 to 3.9 ± 1.9 µm for R1-D30 nanocomposites. However, it is very likely that in both cases there also are submicron-sized aggregates that cannot be properly resolved by EDX mapping, so their actual average size may be even smaller.

### 2.3. Mechanical Properties of 3D Printed Nanocomposites

The mechanical properties of the nanocomposites were evaluated by means of tensile testing, as presented in Figure S10 (Supporting Information), and collected in **Figure 6** and **Table 2**. The stiffness (Young's modulus) of the BTO nanocomposites increased when compared to the pristine R1 resin (+ 19% for R1-B5 and + 7% for R1-B35), but their tensile strength (−2% for R1-B5 and −45% for R1-B35) and elongation at break (−40% for R1-B5 and −70% for R1-B35) decreased significantly, especially in the case of the R1-B35, which presents the lowest strength and elongation among all the nanocomposites studied. The lack of compatibility between the inorganic BTO NPs and the organic resin R1 likely contributes to an increased number of fracture points. The agglomeration of incompatible inorganic fillers often results in higher stiffness (Young's modulus) while significantly reducing the material's elongation at break, thereby making it more brittle.[39,40] This result was anticipated, since these printed nanocomposites displayed BTO aggregates visible to the naked

ADVANCED
SCIENCE NEWS
www.advancedsciencenews.com

ADVANCED
FUNCTIONAL
MATERIALS
www.afm-journal.de

Figure 5. SEM micrographs of 3D printed a) R1; b) R1-D5 and c) R1-D30. EDX mappings of a), b) and c) are shown in d), e) and f) respectively. Yellow arrows show different locations with particles that do not contain neither Ba nor Ti.

eye. BTO-DDA nanocomposites exhibited a slight increase in stiffness for R1-D5 (+3%). However, a general decreasing trend was observed for all the mechanical properties studied, although the tensile strength and elongation at break decreased to a lesser extent compared to BTO nanocomposites. Specifically, the elongation at break values remained ≈4% strain for all the BTO-DDA nanocomposites tested, with relatively high standard deviations, indicating that these differences are not particularly significant. This suggests that the presence of BTO-DDA does not drastically weaken the polymer network, thereby demonstrating the role of DDA as a compatibilizer. Other researchers have reported similar findings regarding the mechanical properties of polymer-BTO nanocomposites using different matrices. For example, Khatri et al. found no significant differences in Young's modulus and tensile strength in ABS composites with 5 vol.% BTO NPs (≈38 wt.%) prepared by extrusion.[41] Similarly, Zhang et al. did not observe any significant improvement in tensile strength in 1 vol.% (5 wt.%) BTO composites prepared in a cel-

lulose matrix via solvent casting.[42] Wondu et al. noted a slight increase in tensile strength, from ≈6 to 8 MPa, in PBAT composites where the BTO NPs were previously functionalized to enhance their compatibility with the polymer matrix.[43] In their study, a fixed amount of 40 vol.% BTO NPs (ca. 78 wt.%) was used. These concentrations are much higher than those used in our study, and none of these cases showed significant enhancement of mechanical properties. Like in our work, the primary purpose of using BTO NPs in these studies was to impart functional properties rather than to improve the mechanical performance of the material. Therefore, it should be emphasized that BTO is principally employed to confer piezoelectric properties to the polymer matrix, not to enhance its mechanical properties. Hence, that the mechanical properties decrease very slightly, having non-significant differences between the pristine resin R1 and the 0.5 – 1.0 wt.% BTO-DDA nanocomposites, may be considered as proof of good compatibility between the filler and the polymer matrix, since the presence of BTO-DDA does not virtually
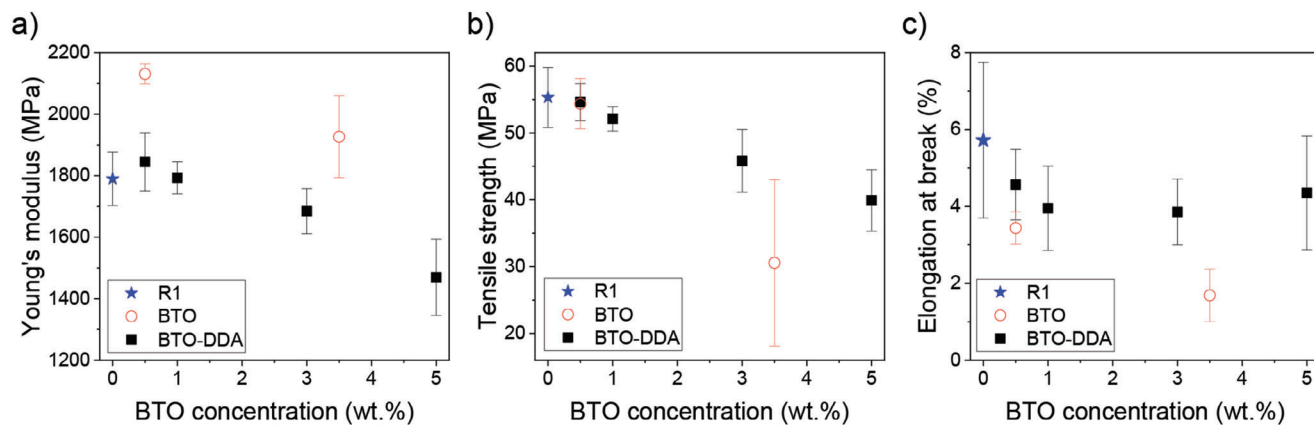
Figure 6. Tensile testing of R1 nanocomposites. a) Young's modulus; b) tensile strength and c) elongation at break of BTO and BTO-DDA nanocomposites.

ADVANCED
SCIENCE NEWS

www.advancedsciencenews.com

ADVANCED
FUNCTIONAL
MATERIALS

www.afm-journal.de

Table 2. Mechanical and piezoelectric properties of nanocomposites prepared with resin R1. Tensile testing results are expressed as mean ± SD, obtained by testing five replicate samples for each formulation.

Sample	Young's Modulus [MPa]	Tensile Strength [MPa]	Elongation at Break [%]	Average d33 [pC/N][a]
R1	1790 ± 90	55.3 ± 4.5	5.7 ± 2.0	0.4
R1-B5	2130 ± 30	54.3 ± 3.7	3.4 ± 0.4	–
R1-B35	1920 ± 130	30.6 ± 12.4	1.7 ± 0.7	–
R1-D5	1840 ± 90	54.6 ± 2.8	4.6 ± 0.9	15.3
R1-D10	1790 ± 52	52.1 ± 1.8	3.9 ± 1.1	21.1
R1-D30	1680 ± 70	45.8 ± 4.7	3.8 ± 0.8	40.4
R1-D50	1470 ± 120	39.9 ± 4.6	4.3 ± 1.5	2.0

[a] Measured for samples printed with layer thickness of 0.05 mm and poled at 1.2 kV.

interfere with the polymer network. This does not happen, however, in the case of the unmodified BTO nanocomposites.

Given the promising results obtained with the BTO-DDA nanocomposites using R1, a similar set of nanocomposites were prepared using flexible resins R2 and R3 and BTO-DDA NPs (Tables S1 and S2 and Figures S11 and S12, Supporting Information). The maximum concentration of BTO-DDA NPs used for these nanocomposites was 2.3 and 3.0 wt.% for R2 and R3, respectively, since higher BTO-DDA contents led to larger aggregates and poorer mechanical properties in general. Following a similar protocol than with R1, standard specimens for mechanical testing and piezoelectric discs were done and their mechanical properties were also studied. Flexible composites were printed with resin R2, and the effect of the addition of BTO-DDA nanoparticles on the flexural modulus of the printed nanocomposites was assessed (Table S3 and Figure S13, Supporting Information), revealing a slight increase in the material's flexural rigidity with increasing BTO content. However, even at 2.3 wt.% loading, the printed composites displayed high deformation at break, higher than the physical limit of the flexural testing machine (> 25%). Due to their intermediate mechanical behavior, R3 nanocomposites were tested in terms of both tensile and flexural properties (Table S4 and Figure S14, Supporting Information). In this case, elongation at break and tensile strength were more significantly affected by the increase in BTO-DDA content since both parameters decreased by ≈50% of their original value when BTO-DDA was added at 3 wt.%. Nonetheless, a slight increase in the flexural modulus was observed with increasing BTO-DDA content as previously observed for resin R2, suggesting an increase in the rigidity of the polymer composite material. These results suggest that resin R1 is characterized by the best matrix-filler compatibility when compared to a flexible commercial alternative (such as R2) and to custom-made acrylate mixtures (such as R3). In a previous work, our group reported fatty acid-functionalized cellulose nanocrystals as a reinforcing nanofiller for rigid VP resin systems, showing the highest matrix-filler compatibility at low nanocellulose loadings (up to 2 wt.%).[18] By comparing the two approaches, it look clear how the long aliphatic chains that were used to increase the resin compatibility in both cases (the C12 chain of DDA in this work and the fatty acid mixture previously used on cellulose nanocrystals) express the best of their potential in rigid systems, probably due to the formation of

strong hydrophobic interaction between the aliphatic chains and the highly crosslinked polymer networks. Previous studies reported similar effects with different nanomaterials such as montmorillonite, and nanofillers surface-modified with long aliphatic chains displayed optimal compatibility at low nanofiller loadings in rigid polymer networks.[44,45]
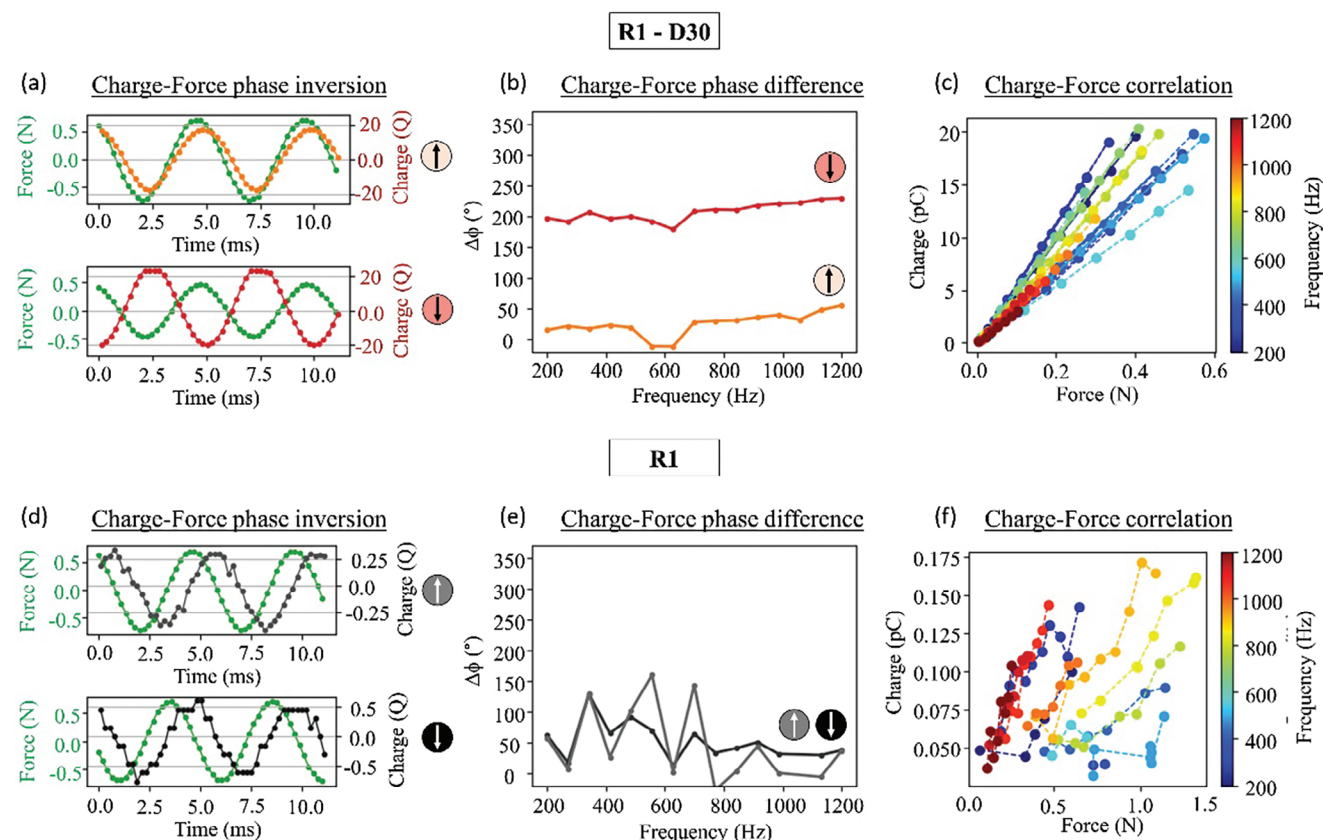
2.4. Piezoelectric Characterization of 3D Printed Nanocomposites

Prior to measuring the piezoelectric properties of the BTO nanocomposites, the samples were subjected to a poling procedure by applying a potential difference (1.0 and 1.2 kV) around the Curie temperature of the BTO NPs (120 °C) in order to align their dipoles and confer the nanocomposites with piezoelectric behavior. However, the nanocomposites prepared with R2 and R3 exhibited semiconducting behavior while poling, which compromised the efficiency of the poling and would potentially damage the equipment. Although all the resins exhibited non-conductive behavior at room temperature (**Table 3**), it is true that both flexible resins, R2 and R3 are some orders of magnitude more conductive than R1. This residual conductivity, probably related to the higher mobility of ionic residues produced by the photodegradation of the radical photoinitiator in the less crosslinked polymer network that characterizes flexible photopolymers, prejudiced the performances of the poling step. In light of these findings, and considering the better compatibility of BTO-DDA with resin R1 assessed by mechanical testing, the piezoelectric studies were focused on BTO-DDA nanocomposites prepared using R1 as matrix.

The piezoelectric characterization was focused on BTO-DDA nanocomposites prepared using R1 as matrix. The first objective was to prove that the incorporation of BTO nanoparticles successfully provided piezoelectric properties to the printed discs. Second, a comparison has been carried out, to study how the piezoelectric behavior is affected by the BTO-DDA loading, the thickness of the printing layer and the potential difference applied during the poling process. The typical property that identifies a piezoelectric material is the correlation between the applied force and the resulting charge accumulated at the two opposite sides. Such correlation is characterized by two features: directionality and linearity. In fact, the poling process provides a polarization to the randomly oriented electrical dipoles of the NPs and, therefore, the force-induced electrical field results to be always in the same direction: negative charges always on one side, and positive on the other. For this reason, after the poling process, one of the samples (R1-D30) was subjected two times to piezoelectric characterization, by switching its upper and lower side. As can be seen in **Figure 7a**, in the first orientation the sinusoidal charge accumulation is in phase with the applied force, while a phase inversion of ≈180° is observed after the sample's

Table 3. Electrical conductivity of pristine resins R1-R3 measured at room temperature.

Resin	Electrical Conductivity [S cm^{-1}]
R1	$8.5 \cdot 10^{-17}$
R2	$5.3 \cdot 10^{-13}$
R3	$4.7 \cdot 10^{-15}$

ADVANCED
SCIENCE NEWS
www.advancedsciencenews.com

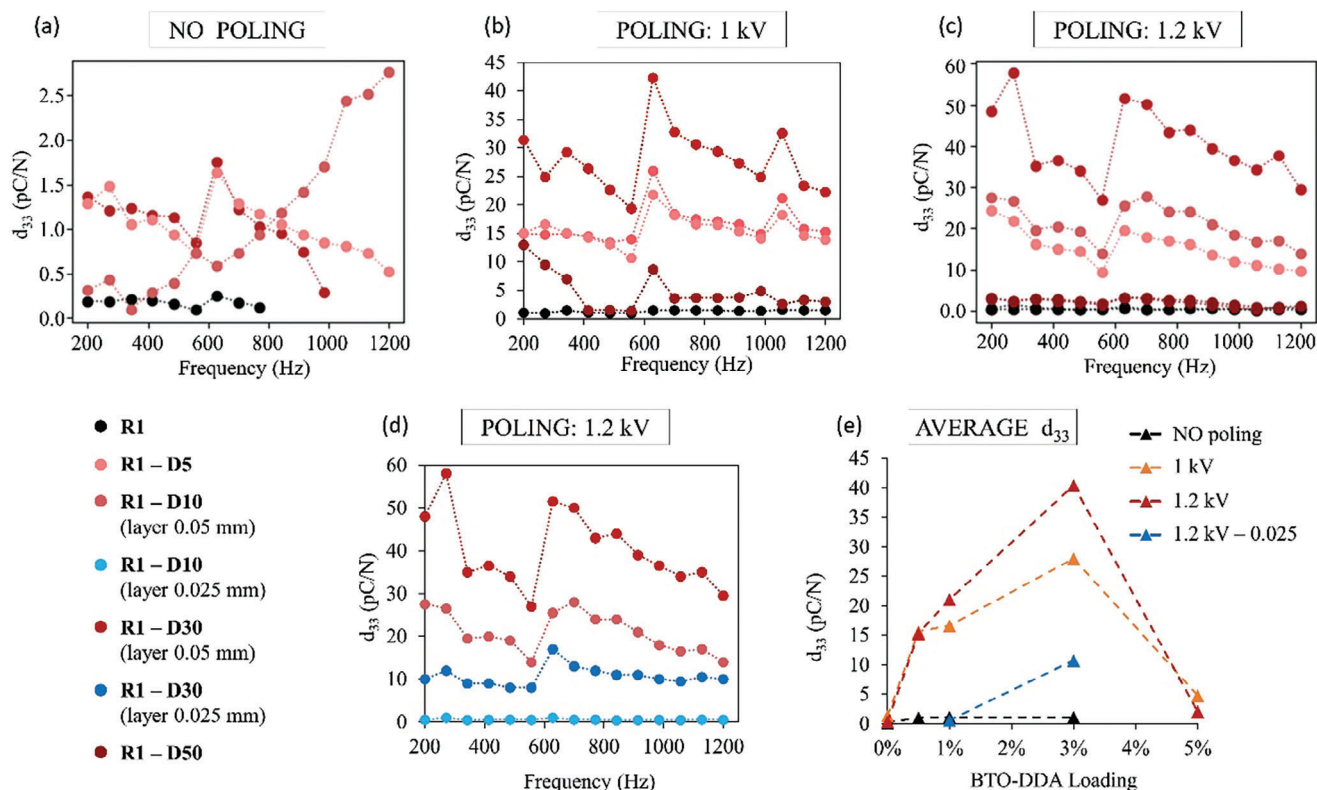ADVANCED
FUNCTIONAL
MATERIALS
www.afm-journal.de

Figure 7. a) Charge-force phase inversion, b) phase difference and c) charge-force correlation obtained from the piezoelectric characterization of R1-D30 samples; d) Charge-force phase inversion, e) phase difference and f) charge-force correlation obtained from the piezoelectric characterization of R1 samples.

switching. Figure 7b plots the phase delay $\Delta\phi$ for all the tested frequencies and it can be seen how it undergoes a clear inversion of 180° in all the cases. This result proves that the charge accumulation is due to a directional piezoelectric effect, rather than non- directional triboelectric phenomena. A further proof is reported in Figure 7c, where the accumulated charge is linearly correlated with the applied forces, over a wide range of frequencies, up to 20 pC for ca. 0.4–0.6 N. Lastly, Figure 7d–f show the results obtained with a printed sample without piezoelectric nanoparticles. As can be seen, the accumulated charge is much lower (up to ca. 0.2 pC), not linearly correlated with the applied force and there is not a clear phase inversion. Therefore, these experiments proved with certainty how the printed nanocomposite materials display a piezoelectric effect, which is provided by the incorporation of the BTO-DDA nanoparticles.Then, more piezoelectric characterizations have been carried out on several samples, in order to study how the piezoelectric behavior is affected by the BTO-DDA loading, the thickness of the printed layers, and the potential difference applied during the poling process. Such evaluation was conducted by comparing, for each sample, the d_{33} coefficient, which correlates the accumulated charge (Coulomb) to the applied force (Newton). The obtained values for the d_{33} coefficients are reported in Tables S5–S8 (Supporting Information) and represented graphically in **Figure** 8. Initially, not poled samples with different amounts of BTO-DDA (0.0, 0.5, 1.0, 3.0, 5.0 wt.%)

have been tested over a range a frequency from 200 to 1200 Hz. As can be seen in Figure 8a, in all the cases the d_{33} coefficient was lower than 2.5 pC/N and it was shown no specific correlation with the BTO loading, proving that the lack of a poling process prevents good piezoelectric behavior. Then, the same characterization was performed on samples that underwent poling at 1.0 or 1.2 kV and the results are shown in Figure 8b,c. The samples with no BTO-DDA basically showed no piezoelectric effect, while the d_{33} values increased with the BTO-DDA loading up to the 3.0 wt.%, up to values higher than 50 pC/N, which is a remarkable value considering the small amount of the employed piezoelectric nanoparticles. In fact, such values are much higher than other d_{33} obtained for nanocomposite materials with low BTO loadings (for example, d_{33} = 5 pC/N for 20% BTO in PDMS),[34] and comparable to other materials where piezoelectric nanoparticles have been employed in much higher mass ratios (as reported in the introduction). Probably, the efficient employment of the VAT manufacturing process, together with the chemical affinity between nanoparticles, ligands and polymeric matrix, allowed to obtain a nanocomposite material characterized by a good combination of NPs dispersion, mechanical properties (so that the applied force is transmitted to the NPs, rather than absorbed by the matrix) and also dielectric properties (so that the NPs piezoelectricity would not be countered by an opposite inner polarization of the matrix). Besides, the samples with the highest loading

**ADVANCED
SCIENCE NEWS**

www.advancedsciencenews.com

**ADVANCED
FUNCTIONAL
MATERIALS**

www.afm-journal.de

Figure 8. Results of the piezoelectric characterization of the 3D printed nanocomposites discs. The d_{33} coefficient has been calculated and plotted for each frequency from 200 to 1200 Hz; a) not poled samples; b) samples poled at 1.0 kV; c,d) samples poled at 1.2 kV; e) plot reporting the average d_{33} obtained from the previous experiments.

of 5.0 wt.% displayed very low piezoelectric behavior. This result can be attributed to several factors, including non-uniform dispersion, nanoparticle aggregation, and interactions with the polymer matrix. In fact, at high concentrations, nanoparticles tend to aggregate into larger clusters, reducing the effective transmission of piezoelectric properties. This can lead to a "shielding effect," where interactions between nearby particles lower the internal electric field they generate. Additionally, higher concentrations can alter the interaction between the matrix and nanoparticles, affecting the dipole orientation and diminishing the overall piezoelectric effect. which is likely due to a non-optimal dispersion of the nanoparticles inside the resin matrix. Other references can be found in literature, where polymer-$BaTiO_4$ nanocomposites displayed d_{33} peak values at intermediate NPs concentrations.[46,47] Therefore, 3.0 wt.% resulted to be the best BTO-DDA loading to have a good dispersion and a high piezoelectric response. It was also found out how higher applied potential during the poling process (1.2 kV rather than 1.0 kV) led to higher d_{33} coefficient. The observed trend variation at low frequencies (200 – 400 Hz) can be ascribed to a complex non-linear correlation between the applied poling potential and electro-mechanical behavior at different frequencies. It should be noticed how it was possible to perform a quantitively piezoelectric characterization, thanks to an accurate measure of the piezoelectric coefficient of several samples in a wide range of frequency. Figure 8d shows a comparison between the nanocomposite discs with a different thickness of the printing layer: 0.100 and 0.025 mm. As can be seen,

the lower layer thickness resulted in a lower d_{33} coefficient. This finding can have to possible explanations: a lower thickness of the printing layer means a higher number of layer junctions, possibly resulting in a higher "fragmentation" of the printed discs. Also, the resin's polymerization kinetic can be slightly changed by different layer heights and this can have an effect on the BTO-DDA dispersion in the matrix. The plot in Figure 8e summarizes the detected trend of the d_{33} coefficient as a consequence of the BTO loading, poling applied potential and printing layer thickness. Lastly, the long-term stability of the materials has been investigated. To this purpose, a specimen of R1D30 (0.05 mm) was poled at 1.2 kV and tested at 1000 Hz, two years after its production. The d_{33} coefficient resulted to be of 33.7 pC/N, very similar to the previous value of ca. 35 pC/N. This result constituted robust evidence of the long-term stability of the printed piezoelectric nanocomposites. The corresponding graph can be found in Figure S15 (Supporting Information).

3. Conclusion

In conclusion, in this work we reported the formulation of lipophilic BTO nanoparticles (BTO-DDA) into rigid and flexible resins for vat photopolymerization, to produce nanocomposites with low BTO contents (0.5–5 wt.%). At first, it was observed that the mechanical properties of 3D-printed materials were not significantly affected by the introduction of the surface-modified nanomaterials, but when BTO-DDA was replaced with pristine

BTO NPs a significant reduction in tensile strength (−26% at 0.5 wt.% loading) was observed together with an increase in the stiffness of the material (+ 16% at 0.5 wt.% loading), once again revealing the importance of surface functionalization in the design of functional nanocomposites. Then, 3D printed materials were subjected to a poling step, and their piezoelectric properties were determined by measuring the accumulated charge as a function of the frequency of the applied force, for different BTO-DDA concentrations. A first set of measurements revealed the importance and the effectiveness of the poling step, since non-poled samples displayed piezoelectric d_{33} coefficients in the 0.5 – 2.5 pC/N range, while poled samples were characterized by d_{33} values reaching 50 pC/N for samples containing 3.0 wt.% BTO-DDA. This outstanding value is around one third of the piezoelectric coefficient reported for bulk BTO, and ten times higher than the one previously reported for the same nanoparticles dispersed in PDMS at concentrations of 20 wt.%. Finally, the effect of AM layer thickness on the piezoelectric properties of the 3D printed materials were evaluated, revealing that lower layer heights corresponded to lower piezoelectric performances. Overall, this study revealed how vat photopolymerization-based AM approaches can be efficiently employed for the preparation of piezoelectric materials with good spatial resolution, versatile mechanical properties, and good piezoelectricity, finding possible applications in the manufacturing of wearable sensors and energy harvesting devices.

4. Experimental Section

All chemicals were purchased from Sigma–Aldrich (St. Louis, MO, USA) and used as received. Dopamine dodecylamine (DDA, N-(3,4-dihydroxyphenethyl)dodecanamide) was synthetized as previously described.[34]

Synthesis and Characterization of BTO-DDA NPs: Piezoelectric barium titanate nanoparticles (BTO NPs) were prepared as originally described by Yoon et al.,[48] exploiting the solvothermal hydrolysis of Ti(iPrO)$_4$ in isopropanol using Ba(OH)$_2$ · 8H$_2$O as both the barium and water source. Then, DDA-functionalized BTO NPs (BTO-DDA NPs) were prepared as previously described.[34] In order to confirm the structure and composition of the nanomaterial reported by Villa et al in 2021, the particles were characterized using X-ray diffraction (XRD), transmission electron microscopy (TEM) and thermogravimetric analysis (TGA). XRD analysis was performed using a Philips PW 1050/81 spectrometer with a PW 1710 chain counting. A nickel filter of 0.15 418 mm was used to make monochromatic the Cu(Kα) radiation. The acquisition region was 5° < 2 theta < 80°, with steps of 0.1° and count of intensity every 2 s. The range of analysis was 20° < 2 theta < 80° with a scanning rate of 0.05°/s and time-per-step = 1 s. Transmission electron microscopy (TEM) analysis was performed on a TEM/STEM FEI TECNAI F20 at 200 keV by depositing a drop of nanoparticles suspension on a carbon-coated copper grid and then dried at room temperature. STEM pictures were recorded using an High Angle Annular Dark Field (HAADF) detectors. TGA was performed on unmodified BTO NPs, on the DDA ligand and on BTO-DDA NPs using a Mettler Toledo TGA 2 Star system. The sample has been heated from 25 to 600 °C with a heating rate of 10 °C min^{-1} and 50 mL min^{-1} N$_2$ flow, then switched in air for the oxidation of carbonaceous residues.

Formulation and 3D Printing of BTO-Loaded Resins: The nanocomposite precursors were prepared by mixing the BTO NPs in 50–60 g of resin by varying the BTO content from 0.5 to 10 wt.%. Three different resins were used as polymer matrix to disperse the BTO NPs: Commercially available XYZ UV-curable Clear Resin (resin R1), XYZ UV-curable Flexible Resin (resin R2), and a previously tested flexible resin containing ethy-

lene glycol phenyl ether acrylate (89 wt.%, EGPEA), 1,6-hexanediol diacrylate (9 wt.%, HDDA), diphenyl (2,4,6-trimethylbenzoyl) phosphine oxide (1 wt.%, MAPO) and phenyl bis(2,4,6-trimethylbenzoyl) phosphine oxide (1 wt.% BAPO) (resin R3).[49] In all cases the BTO NPs were dispersed by mixing them with the resin under gentle stirring at 200 rpm to minimize the formation of air bubbles and the dispersions were sonicated for 10 min in a USC500T Ultrasonic Cleaner. Rheological analysis was performed on an Anton-Parr MCR102 modular compact rheometer with a DPP25-SN0 geometry, indicating a double plate geometry with a diameter of 25 mm. UV–vis spectra were recorded using a Varian Cary 50 Conc spectrophotometer. The range between 300 and 800 nm was monitored with a scan rate of 10 nm s^{-1}. Fourier-transform infrared (FTIR) spectroscopy analysis was carried out using a Bruker Alpha spectrophotometer via attenuated total reflectance (ATR) mode in the range of 4000–650 cm^{-1} with a spectral resolution of 4 cm^{-1}. Then, the mixture was poured into the vat of the SL printer (Nobel 1.0, XYZprinting Inc.) and different objects were manufactured using a 405 nm laser with an output power of 100 mW, a XY resolution of 300 µm and a layer height of 25–100 µm. Computer-assisted design (CAD) files of 1BA tensile testing specimens according to ISO 527, bending testing specimens according to ISO 178, flat discs of 15 mm diameter and 1 mm thickness and complex structures such as hollow cubic lattices (10 × 10 × 10 mm^3) were loaded using the XYZware Nobel software. The 3D-models were converted into a GCODE file, suitable for 3D-printing. The printed objects were then separated from the printer platform and washed with isopropyl alcohol for at least 15 min. Post-processing of the samples was carried out for 60 min in a chamber equipped with a 405 nm light source and a power of 1.25 mW cm^{-2} (FormCure, Formlabs), previously heated to 60 °C. The mechanical properties of the printed composites were measured in a Shimadzu AGS-X universal testing machine. Tensile and bending testing of the specimens were carried out at 1 mm min^{-1}, in agreement with ISO 178 and ISO 527, respectively. Scanning electron microscopy (SEM) measurements were done in a Nova NanoSEM 450 equipped with an energy-dispersive X-ray (EDX) microanalysis detector. Samples were previously coated with a few nm Au layer in a Balzers SCD 004 sputter coater. The electrical conductivity of the materials was measured in a Keithley 6517B conductivity meter using a voltage of 500 V in agreement with ASTM D257.

Poling and Piezoelectric Characterization of 3D Printed Nanocomposites: The piezoelectric studies were focused on BTO-DDA nanocomposites prepared using R1 as the matrix. The samples underwent a poling process to align the randomly oriented dipoles of the piezoelectric nanoparticles. The samples have been placed between two metal plates, kept at 140 °C and subjected to a poling applied potential of 1.0 or 1.2 kV for 2 h. The applied potential was kept while cooling the system down to 110 °C (2 h) and then to room temperature (another 2 h). The whole process was conducted at a pressure of 3×10^{-5} bar. After the poling process, the samples were left to rest for 24 h, before further testing.

The experimental setup and procedures employed for the piezoelectric characterization are the same reported in the work of Villa et al.[34] A vertical oscillating force is applied perpendicularly to the sample by means of an electromechanical exciter (Visaton EX 60S loudspeaker), while the force is measured by a force sensor (TE Connectivity FS2050-000X-1500-G) and the output charge is collected by a dedicated electronic circuit. This allowed to stimulate the samples in a frequency range from 200 to 1200 Hz, with peak forces up to 0.6 N. The charge accumulated by the samples has been collected with two electrodes: the top was fastened to the force sensor head, while the bottom electrode was secured to the vibrating bottom surface. The force and charge electronic signals were collected and converted by an Arduino Mega ADC, and then analyzed by a dedicated LabVIEW program. A charge amplifier circuit, provided with changeable feedback capacitive elements (C$_f$, from 4.7 to 150 µF), was employed to extract the charge from the samples and to convert it into a potential difference (ΔV_{output}). Then, the accumulated piezoelectric charge (Q) was calculated as reported in Equation (1). The d_{33} piezoelectric coefficient was finally obtained according to Equation (2).

$$Q\ (C) = \Delta V_{output}\ (V) \times C_f\ (F) \tag{1}$$

$$d_{33} (C/N) = Q (C) / F (N) \quad (2)$$

Statistical Analysis: The presented mechanical properties (Young's modulus, elongation at break and tensile strength) are obtained according to ISO 527 for tensile testing and ISO 178 for bending testing, and the results were averaged over five independent measurements on independently printed specimens. Results are presented in Figure 6 and Table 2 as mean ± SD. Electrical conductivity measurements were performed according to ASTM D257 and the results were averaged over three independent measurements on independently printed specimens. Mean values are presented in Table 3. The data reported in Figure 7 have been obtained from two representative specimens R1-D30 and R1. All data presented in Figure 8a–d come from a single dataset (Dataset A). To enhance statistical robustness, two additional datasets (Datasets B and C) were collected. By combining all three datasets, the mean values for each formulation was calculated, poling condition, and tested frequency. The standard deviations in all cases were less than 2 pC/N. Consequently, Dataset A was considered representative of all three datasets and is the one reported in the manuscript. Figure 8e displays the d_{33} coefficients of the different samples of Dataset A, averaged across the tested frequencies. The corresponding values and standard deviations are provided in Table S8 (Supporting Information).

Supporting Information

Supporting Information is available from the Wiley Online Library or from the author.

Acknowledgements

Conflict of Interest

The authors declare no conflict of interest.

Data Availability Statement

The data that support the findings of this study are available from the corresponding author upon reasonable request.

Keywords

[1] S. K. Adapa, Jagadish, *JOM* **2023**, *75*, 920.
[2] G. Chyr, J. M. DeSimone, *Green Chem.* **2023**, *25*, 453.
[3] H. Hegab, N. Khanna, N. Monib, A. Salem, *Sustain. Mater. Technol.* **2023**, *35*, e00576.
[4] N. Top, I. Sahin, S. K. Mangla, M. D. Sezer, Y. Kazancoglu, *Int. J. Prod. Res.* **2023**, *61*, 4450.
[5] G. Prashar, H. Vasudev, D. Bhuddhi, *Int. J. Interact. Des. Manuf.* **2023**, *17*, 2221.
[6] N. Shahrubudin, T. C. Lee, R. Ramlan, *Procedia Manuf.* **2019**, *35*, 1286.
[7] A. Al Rashid, W. Ahmed, M. Y. Khalid, M. Koç, *Addit. Manuf.* **2021**, *47*, 102279.
[8] F. Zhang, L. Zhu, Z. Li, S. Wang, J. Shi, W. Tang, N. Li, J. Yang, *Addit. Manuf.* **2021**, *48*, 102423.
[9] A. Medellin, W. Du, G. Miao, J. Zou, Z. Pei, C. Ma, *J. Micro Nano-Manuf.* **2019**, *7*, 031006.
[10] M. Shah, A. Ullah, K. Azher, A. U. Rehman, W. Juan, N. Aktürk, C. S. Tüfekci, M. U. Salamci, *RSC Adv.* **2023**, *13*, 1456.
[11] H. A. Colorado, E. I. Gutierrez-Velasquez, L. D. Gil, I. L. de Camargo, *Adv. Compos. Hybrid Mater.* **2024**, *7*, 1.
[12] Y. Wang, A. P. Delarue, I. M. McAninch, C. J. Hansen, E. J. Robinette, A. M. Peterson, *ACS Appl. Polym. Mater.* **2022**, *4*, 6477.
[13] J. Li, L. Wang, L. Dai, L. Zhong, B. Liu, J. Ren, Y. Xu, *J. Mater. Sci.* **2018**, *53*, 1874.
[14] M. Lebedevaite, A. Gineika, V. Talacka, K. Baltakys, J. Ostrauskaite, *Compos. A Appl. Sci. Manuf.* **2022**, *157*, 106929.
[15] M. Jurinovs, A. Barkane, O. Platnieks, S. Beluns, L. Grase, R. Dieden, M. Staropoli, D. F. Schmidt, S. Gaidukovs, *ACS Appl. Polym. Mater.* **2023**, *5*, 3104.
[16] N. Paunović, J. Marbach, Y. Bao, V. Berger, K. Klein, S. Schleich, F. B. Coulter, N. Kleger, A. R. Studart, D. Franzen, Z. Luo, J. C. Leroux, *Adv. Sci.* **2022**, *9*, 2200907.
[17] Y. Cho, J. Kim, *Polym. Test.* **2023**, *118*, 107898.
[18] M. Maturi, C. Spanu, N. Fernández-Delgado, S. I. Molina, A. Comes Franchini, E. Locatelli, A. Sanz de León, *Addit. Manuf.* **2023**, *61*, 1.
[19] R. Tu, B. Zhang, H. A. Sodano, *Nano Energy* **2022**, *97*, 107175.
[20] R. Tao, J. Shi, F. Granier, M. Moeini, A. Akbarzadeh, D. Therriault, *Appl. Mater. Today* **2022**, *29*, 101596.
[21] Y. Wu, Y. Ma, H. Zheng, S. Ramakrishna, *Mater. Des.* **2021**, *211*, 110164.
[22] C. Chen, X. Wang, Y. Wang, D. Yang, F. Yao, W. Zhang, B. Wang, G. A. Sewvandi, D. Yang, D. Hu, *Adv. Funct. Mater.* **2020**, *30*, 2005141.
[23] L. Wang, Y. Ma, K. Wang, Y. Ma, K. Wang, B. Lu, L. Niu, X. Li, *Sensors Actuators A Phys* **2023**, *362*, 114586.
[24] W. Wang, J. Sun, B. Guo, X. Chen, K. P. Ananth, J. Bai, *J. Eur. Ceram. Soc.* **2020**, *40*, 682.
[25] X. Hu, X. Li, K. Yan, X. Qi, W. Chen, D. Wu, *Ceram. Int.* **2021**, *47*, 32376.
[26] K. Tewatia, A. Sharma, M. Sharma, A. Kumar, *Mater. Today Proc.* **2021**, *44*, 4548.
[27] V. Buscaglia, C. A. Randall, *J. Eur. Ceram. Soc.* **2020**, *40*, 3744.
[28] H. Li, Y. Song, T. Kim, M. Lee, S. Lim, *Macromol. Mater. Eng.* **2022**, *307*, 2200235.
[29] Z. Wang, Z. Liu, G. Zhao, Z. Zhang, X. Zhao, X. Wan, Y. Zhang, Z. L. Wang, L. Li, *ACS Nano* **2022**, *16*, 1661.
[30] J. Jiang, L. Wan, L. Li, P. Li, *Macromol. Rapid Commun.* **2024**, *45*, 2300619.
[31] L. He, X. Wang, F. Fei, L. Chen, X. Song, *Addit. Manuf.* **2021**, *48*, 102407.
[32] A. Sotov, A. Kantyukov, A. Popovich, V. Sufiiarov, *Ceram. Int.* **2021**, *47*, 30358.
[33] C.-L. Liu, Q. Du, C. Zhang, J.-M. Wu, G. Zhang, Y.-S. Shi, *Addit. Manuf.* **2022**, *56*, 102940.
[34] S. M. Villa, M. Maturi, T. Santaniello, L. Migliorini, E. Locatelli, M. Comes Franchini, P. Milani, *Sensors Actuators A Phys* **2021**, *332*, 113196.
[35] E. K. Al-Shakarchi, N. B. Mahmood, *J. Mod. Phys.* **2011**, *02*, 1420.

[36] S. M. Villa, V. M. Mazzola, T. Santaniello, E. Locatelli, M. Maturi, L. Migliorini, C. Lenardi, M. C. Franchini, P. Milani, I. Monaco, C. Lenardi, M. Comes Franchini, P. Milani, *ACS Macro Lett.* **2019**, *8*, 414.

[37] J. Loste, J.-M. Lopez-Cuesta, L. Billon, H. Garay, M. Save, *Prog. Polym. Sci.* **2019**, *89*, 133.

[38] V. S. D. Voet, T. Strating, G. H. M. Schnelting, P. Dijkstra, M. Tietema, J. Xu, A. J. J. Woortman, K. Loos, J. Jager, R. Folkersma, *ACS Omega* **2018**, *3*, 1403.

[39] Y.-T. Choi, S. B. Kim, S. J. Lee, G.-T. Kim, E.-H. Park, E.-S. Park, *Compos. B Eng.* **2017**, *114*, 268.

[40] M. C. Kuo, C. M. Tsai, J. C. Huang, M. Chen, *Mater. Chem. Phys.* **2005**, *90*, 185.

[41] B. Khatri, K. Lappe, M. Habedank, T. Mueller, C. Megnin, T. Hanemann, *Polymers* **2018**, *10*, 666.

[42] C. Zhang, Y. Yin, Q. Yang, Z. Shi, G.-H. Hu, C. Xiong, *ACS Sustain. Chem. Eng.* **2019**, *7*, 10641.

[43] E. Wondu, G. Lee, J. Kim, *Polym. Test.* **2024**, *135*, 108447.

[44] H. Eng, S. Maleksaeedi, S. Yu, Y. Y. C. Choong, F. E. Wiria, C. L. C. Tan, P. C. Su, J. Wei, *Procedia Eng.* **2017**, *216*, 1.

[45] Z. Weng, Y. Zhou, W. Lin, T. Senthil, L. Wu, *Compos. A Appl. Sci. Manuf.* **2016**, *88*, 234.

[46] H. Aldulaimi, G. Pircheraghi, A. Nemati, *Polym. Compos.* **2024**, 9919.

[47] Y. P. Su, L. N. Sim, H. G. L. Coster, T. H. Chong, *J. Membr. Sci.* **2021**, *640*, 119861.

[48] S. Yoon, S. Baik, M. G. Kim, N. Shin, *J. Am. Ceram. Soc.* **2006**, *89*, 1816.

[49] J. Borrello, P. Nasser, J. C. Iatridis, K. D. Costa, *Addit. Manuf.* **2018**, *23*, 374.